Cracking in autoclaved aerated concrete: Experimental investigation and XFEM modeling



*Original*
Cracking in autoclaved aerated concrete: Experimental investigation and XFEM modeling / Ferretti, Daniele; Michelini, Elena; Rosati, G.. - In: CEMENT AND CONCRETE RESEARCH. - ISSN 0008-8846. - 67:(2015), pp. 156-167. [10.1016/j.cemconres.2014.09.005]

*Availability:*
This version is available at: 11381/2765338 since: 2021-10-21T15:35:49Z

*Publisher:*
Elsevier Ltd

*Published*
DOI:10.1016/j.cemconres.2014.09.005

# Cracking in autoclaved aerated concrete: experimental investigation and XFEM modeling

**D. Ferretti[1] *, E. Michelini[1] and G. Rosati[2]**

[1] *Department of Civil, Environmental, Land Management Engineering and Architecture, University of Parma, P.co Area delle Scienze 181/A, 43124 Parma, Italy*
[2] *Department of Civil and Environmental Engineering, Politecnico di Milano, Piazza L. Da Vinci 32, 20133 Milano, Italy*
* Corresponding author. Tel. +39 0521 905943; fax +39 0521 905924.
E-mail address: daniele.ferretti@unipr.it (D. Ferretti).

**ABSTRACT**

*The paper aims to investigate and model cracking development in beams and deep-beams made of autoclaved aerated concrete (AAC). Fracture mechanics of AAC has been first studied by performing three-point bending tests on beams, similar to those commonly used for ordinary concrete elements. In some of these tests, crack growth has been also monitored by using ESPI laser technique. In this way, it has been possible to calibrate the main parameters of a proper cohesive law by means of extended finite element inverse analysis. Subsequently, cracking tests have been also performed on deep-beams, whose behavior is more representative of full scale walls. To validate the proposed cohesive law, deep-beams experimental behavior has been finally simulated through XFEM.*

**KEYWORDS**

AAC; ESPI; cracking; cohesive model; XFEM.

## 1. INTRODUCTION

In recent years, autoclaved aerated concrete (AAC) has been widely recognized as a high quality, innovative material that has been extensively used for the realization of residential, commercial and industrial buildings.

As known, AAC is a lightweight structural material with interesting sound and thermal insulation properties, so allowing satisfying increasingly stringent building design requirements, whilst ensuring environmental compliance [1, 2]. From a structural point of view, AAC is suitable for the realization of masonry bearing walls of low-to-medium rise buildings, since it offers high fire-resistance, due to its incombustible nature, and adequate mechanical properties, at least for the material with higher density values (corresponding to higher compressive strengths). The structural behavior of AAC − especially under accidental or seismic loads − is also influenced by its toughness, which exerts an important role on its resistance against damage during transport and handling [3]. Fracture toughness is also relevant with respect to cracking, which represents a quite common problem of AAC masonry even under static loads. This problem is particularly significant for AAC internal partitions, due to the deformability of the upper floor, which can lean on them – thus representing an additional, not calculated load – or to that of the bottom floor, which can drag down the wall, connected to it.

The mechanical study of this problem requires the knowledge of material properties, like tensile strength and fracture energy. These latter have been mainly analyzed in the past through experimental tests on compact tension specimens and wedge-splitting specimens, whose results can be found in the technical literature [3-7].

Aim of this work is to investigate cracking development in AAC walls under static loads and, more generally, cracking in AAC structures. To this scope, three point bending tests, similar to those commonly used for ordinary concrete, have been performed on AAC elements, trying to overcome the difficulties related to crack propagation control. More in details, a preliminary set of tests on both AAC beams and deep-beams has been performed under loading control, so as to quantify the statistical variability of material tensile strength. Subsequently, similar specimens have been tested under crack-mouth opening displacement (*CMOD*) control, so as to obtain the complete load-displacement curve and, consequently, the material fracture energy $G_F$. In order to determine a proper cohesive law, crack propagation has been observed by using ESPI technique (Electronic Speckle Pattern Interferometry), which allows to observe the displacement field of a surface illuminated by a laser light with a precision higher than 10 μm. This has permitted to detect the cracking onset and to observe the crack profile. The so obtained results have been then used for calibrating the parameters of a proper cohesive law through an inverse analysis procedure, performing a non-linear extended finite element analysis; this law substantially agrees with those available in the literature, obtained through wedge-splitting tests [4]. Finally, the proposed cohesive law has been adopted in a XFEM model so as to reproduce the experimental cracking growth in a reduced scale AAC wall.

## 2. EXPERIMENTAL TESTS ON AAC

### *2.1 Mechanical characterization of the material*

As already mentioned, the first part of the experimental program aimed to provide a mechanical characterization of the investigated material, by quantifying at the same time the statistical variability of the most important properties. Before testing, all the investigated samples, characterized by an average density $\rho \approx 550$ kg/m$^3$, were cured in laboratory conditions so as to reach relatively low moisture contents. It should be indeed reminded that AAC strength is influenced by several parameters, which are not only related to specimen size and shape, but also to method of pore formation, direction of loading, age, moisture content, characteristics of ingredients adopted in the mix, and method of curing [8, 9].

As known, AAC compressive strength is usually determined on cubes with an edge length of 100 mm, even if cubes with an edge length of 150 mm can be also used according to RILEM [3]; within this range the size of samples does not influence the results. In the technical literature, also cylindrical or prismatic samples are often used (e.g., [10]); in this case, the measured strength is generally lower than that determined on cubes and decreases with increasing sample slenderness (it is approximately 5% lower for slenderness equal to 2-3, [3, 11]). It is also possible to determine the compressive strength by directly testing the block units [3, 12]; the so obtained values may be up to 10% lower than the ones measured on cubes. In this case, the maximum sustainable load of the unit and the corresponding compressive strength is indeed governed by the failure of the weaker side of the specimen.

In this paper, the statistical variability of AAC mechanical properties (strength and deformability parameters in compression) has been investigated with reference to specimens characterized by different shapes and dimensions, so as to understand if the results provided by standard tests can be used to effectively model the behavior of full-scale walls, especially in case of internal partitions. To this scope, the results obtained on "traditional" specimens, that is to say cubes with an edge length of 100 mm and prisms with slenderness equal to 2 (characterized by a 40 mm x 40 mm square basis and an height of 80 mm), have been compared with those provided by non-standard samples, represented by blocks and reduced scale walls. More in details, the attention has been focused on blocks with a loaded area equal to 625 x 100 mm and a height equal to 250 mm, commonly used for the realization of internal partitions, as well as on small AAC walls, with a loaded area equal to 625 x 100 mm and a height equal to 750 mm.

### *2.1.1 Uniaxial compression tests on AAC blocks*

At first, 13 compression tests have been performed on AAC blocks for internal partitions. Before testing, all the specimens have been cured in laboratory conditions for about three months until the reaching of a moisture content lower than 10%. Tests have been carried out at the Material and Testing Laboratory of the AAC Manufacturer Company (in Piacenza, Italy), by using a Metrocom PV50 press working under loading control, with a capacity of the hydraulic actuator equal to 5000 kN and a loading rate of 25 kN/min [13]. The adopted test arrangement is shown in Figure 1; in order to apply a distributed load, a 650 mm long steel rigid beam with I-section has been placed on the top of the specimen. AAC surfaces have been preliminary flattened by sandpaper to eliminate any irregularity and thereby ensure a complete contact between the specimen and the testing apparatus; furthermore, thin cardboard layers have been interposed between the specimen itself and the loading press, so as to minimize the confinement effect due to friction and apply a more uniform state of stress. Three of the 13 specimens have been also instrumented with linear variable displacement transducers (LVDTs, see Fig. 1), in order to measure vertical and horizontal strains, $\varepsilon_V$ and $\varepsilon_H$, so as to determine the material elastic modulus $E$ and the Poisson coefficient $\nu$.

As can be seen in Figure 2a, these tests have highlighted a small variability of compressive strength, due to the homogenous structure of the material. The average value of ultimate load was approximately equal to $P_c$ = 150.5 kN, corresponding to a nominal compressive strength $f_c$ = 2.43 MPa, with a coefficient of variation $CV$ = 0.14. In the most of the examined cases, specimen failure was characterized by a widespread cracking, which was mainly concentrated near one of the external corners (Fig. 2b), in the weaker part of the block. As a matter of fact, because of material preparation process, the behavior in the direction of the rise of the mass during manufacturing – perpendicular to loading direction, for the analyzed specimens – is indeed variable along mould height, since the bottom part is significantly more dense and stronger than the top one [12]; as a consequence, one edge of each tested specimen was necessarily less resistant than the other, so influencing the resultant failure load. From the 3 instrumented tests it has been also possible to indirectly determine both the elastic modulus and the Poisson coefficient, which were respectively equal to $E$ = 1285 MPa and $\nu$ = 0.38, with a coefficient of variation approximately equal to 3%. More in details, the elastic modulus has been evaluated with reference to a stress interval ranging between $0.02f_c$ and $0.33f_c$, according to the procedure included in RILEM Recommendations [3]. The so obtained elastic modulus appears to be quite in agreement with the results provided by other experimental campaigns available in the literature [11,14], as well as with the value derivable from a semi-empirical relation between the elastic modulus $E$ and the compressive strength $f_c$ suggested in [11,14]. By substituting the experimental value of compressive strength, $f_c$ = 2.43 MPa, in this expression, which is here reported for reading convenience (with $f_c$ and $E$ in psi):

$$E = 6500\, f_c^{0.6} \tag{1}$$

a value of $E$ = 1512 MPa can be obtained, which is about 15% higher than the measured one. The same Authors [11,14] also indicates that the modulus of elasticity tested parallel to the direction of rise is 170 MPa to 340 MPa lower than in case of loading perpendicular to the direction of rise.

### *2.1.2 Uniaxial compression tests on small AAC walls*

The performed experimental campaign has also included 7 compression tests on small AAC walls, having the same loaded area as the blocks previously described (625 x 100 mm), but a greater height (750 mm, Fig. 3). These compression tests on small walls have been carried out at the same time as the ones on blocks; as a consequence, the same experimental apparatus has been adopted (Fig. 3b).

As can be seen from Figure 4a, the mean value of compressive strength measured on small walls was very similar to that determined on blocks; in this case, the obtained results were even characterized by a lower scatter (with a coefficient of variation *CV* equal to 7% instead of 14%). The average value of ultimate load was indeed approximately equal to $P_c$ = 148.8 kN, corresponding to a nominal compressive strength $f_c$ = 2.39 MPa. This seems to suggest that specimen geometry exerts only a limited influence on nominal compressive strength. Moreover, the failure mode and the corresponding crack pattern of small walls were very similar to the ones already observed for blocks, since also in this case specimen failure was characterized by a widespread cracking, mainly concentrated near one of the external corners (Fig. 4b). Finally, it can be observed that the elastic modulus, as well as the Poisson coefficient indirectly determined on small walls slightly deviates from those already derived from blocks, being respectively equal to $E$ = 1352 MPa and $\nu$ = 0.38, with a coefficient of variation approximately equal to 4%. In this case, Equation 1 provides a value of the elastic modulus equal to $E$ = 1497 MPa, which is about 10% higher than the measured one.

### *2.1.3 Uniaxial compression tests on AAC cubes and prisms*

Finally, the compressive strength values obtained on blocks and small walls have been compared with those obtained on standard cubes with an edge length of 100 mm [15]. These compression tests have been performed according to UNI EN 772-1 [16] and UNI EN 771-4 [17], by cutting the cubes from AAC bearing masonry blocks (whose dimensions were 625 x 250 x 300 mm), characterized by a moisture content approximately equal to 6% (and then comparable to that of specimens described in the previous paragraphs). The so obtained results are summarized in Figures 5a,b which report the trend of compressive strength values respectively in the vertical – parallel to the applied load − and horizontal directions (lilac histogram, C1-C6 and C1*-C6* samples). On this point, it should be underlined that each reported value has been deduced as the average between the strength of three specimens, respectively cut in the upper, the middle and the lower third of each block (as a consequence, a total amount of 18 specimens have been analyzed in the two directions of load). This has permitted to take into account the effect of density variation along the block. As can be seen, a different direction of load application determines different average strengths (which are about 25% higher in the direction of vertical loads), since they are influenced by the direction of mass expansion during manufacture.

The same graph of Figure 5a also reports the strengths of two more cubes (red bars, C7-C8 samples), which have been directly cut from the central part of block B1 at the end of compression tests described in §2.1.1. The so obtained cube strength values appear to be slightly lower than those obtained from C1-C6 samples, even if the moisture content and effective density were almost the same. In any case, the average cube compressive strength in the direction of vertical load appears to be up to 25% higher than the corresponding one measured on slender blocks if all the specimens of Figure 5a are considered, while it is about 15% higher if only the two cubes cut from block B1 are considered (red bars).

Furthermore, 3 prisms with 40 mm square basis and an height of 80 mm extracted from the same batch of blocks B1-B13 have been tested in compression; also in this case, the specimens have been directly cut from the central part of the blocks. As can be observed from Figure 6a, strength measured on prisms (characterized by a slenderness equal to 2) results about 10% lower than that determined on cubes, as could be expected. In order to obtain the stress-strain curve for AAC in compression, these tests have been performed under displacement control. Longitudinal strains have been experimentally measured by means of 4 LVDTs placed on the 4 edges of each prism. The obtained results have been reported in Figure 6b; for comparison, the same graph also shows the stress-strain curve published in [10] for AAC cylinders with a similar density (respectively equal to 544 kg/m$^3$ for AAC1 and 450 kg/m$^3$ for AAC2). As can be seen, Figure 6b confirms a good agreement between the curves of the two experimental campaigns.

Finally, the obtained results have been summarized in Figure 6c in terms of compressive strength values relative to different geometries and dimensions of the investigated samples. As can be expected, compressive strength determined on prisms is slightly lower than that obtained from standard cubes, being $f_c$ = 2.8 MPa instead of 3.1 MPa (with a *CV* respectively equal to 5% and 7%). Compression tests on blocks and reduced scale walls provide instead almost the same value of compressive strength (around $f_c$ = 2.4 MPa), which is about 20% lower than the value obtained from standard cubes.

### *2.2 Evaluation of AAC tensile strength through three-point bending tests*

In order to evaluate AAC tensile strength and its statistical variability, a preliminary set of three-point bending tests have been carried out on 6 AAC beams having the same geometry as the blocks tested in compression (625 x 100 x 250 mm). Moreover, 7 additional three-point tests have been also performed on AAC deep-beams, having the same geometry as the small walls tested in compression (625 x 100 x 750 mm). Before testing, all the considered specimens have been preliminary cured in laboratory conditions for about three months, until the reaching of moisture content lower than 10%. Tests have been carried out at the Material and Testing Laboratory of the AAC Manufacturer Company (in Piacenza, Italy), by using a Instron 5882 press working under loading control, with a loading rate of 1 kN/min [13]. The test setup is shown in Figure 7. Two specimens of each considered typology (beams and deep-beams) have been instrumented with LVDTs, in order to measure horizontal displacements at their top and bottom edges (Fig. 7a). In case of deep-beams, an additional LVDT has been placed in the central part of specimen side (Fig. 7c). Through these tests it has been possible to determine the failure load in bending for the two examined types of specimens. Subsequently, the flexural tensile strength $f_{ct,fl}$ (also called modulus of rupture) has been indirectly derived from linear finite element analyses. More in details, the performed experimental tests have been numerically modeled by adopting the mechanical properties previously derived from the compression tests, by considering average values between beams and deep-beams ($E$ = 1320 MPa, $\nu$ = 0.38 MPa). The small difference of elastic moduli in the two directions (parallel and perpendicular to the applied load, [14]) has been instead neglected for sake of simplicity.

### *2.2.1 Three-point bending tests on AAC beams*

Three-point bending tests on AAC beams have highlighted a small variability of the failure load in flexure. After the reaching of the peak load, all the specimens were characterized by a brittle failure, with the development of a main crack placed nearly at midspan (Fig. 7b). The mean value of flexural tensile strength, determined though a linear elastic FE inverse analysis, was approximately equal to $f_{ct,fl}$ = 0.6 N/mm$^2$, with a coefficient of variation *CV* of about 7% (Fig. 8a). This value fits quite well the design provisions suggested in [14], where the flexural tensile strength $f_{ct,fl}$ is related to the compressive strength $f_c$ through the expression:

$$f_{ct,fl} = 4.8\ (f_c)^{0.5}, \qquad (2)$$

with $f_{ct,fl}$ and $f_c$ in psi. By substituting the compressive strength determined on blocks ($f_c$ = 2.43 MPa) in this latter equation, a value of $f_{ct,fl}$ = 0.62 MPa can be obtained, which is very similar to the one provided by FE inverse analysis. RILEM provisions [3] suggests instead the following relation between the flexural tensile strength $f_{ct,fl}$ and compressive strength $f_c$:

$$f_{ct,fl} = 0.27 + 0.21\ f_c, \qquad (3)$$

so providing an higher and in some cases unconservative [14] value of flexural tensile strength (for the considered case, $f_{ct,fl}$ = 0.78 MPa). In any case it should be remarked that AAC is slightly stronger in flexural tension if flexural stresses are oriented parallel (rather than perpendicular) to the direction of rise [14].

### *2.2.2 Three-point tests on AAC deep-beams*

The results obtained from three-point tests on AAC deep-beams have confirmed the small variability of the flexural failure load. Also in this case, specimens showed a brittle failure, characterized by the spreading of an inclined main crack, starting from the bottom of the specimen, at a distance approximately ranging from 80 to 150 mm

(105 mm on average) from its external edge (Fig. 7d). As regards flexural tensile strength, a mean value of $f_{ct,fl}$ = 0.76 N/mm$^2$ − quite similar to that determined on AAC beams − with a coefficient of variation *CV* of about 9%, has been deduced from linear elastic FE modeling (Fig. 8b). It should be observed that Equations 2 and 3 provide the same results already obtained for beams, due to the similar values of compressive strength (see §§ 2.1.1 and 2.1.2).

## 3. COHESIVE MODEL AND FRACTURE ENERGY

### *3.1 Experimental evaluation of AAC fracture energy*

As already mentioned, some three-point bending tests on AAC beams have been also repeated under crack-mouth opening displacement (*CMOD*) control, so as to obtain the fracture energy $G_F$ and calibrate a proper cohesive law for the investigated material. These tests have been carried out at the Materials and Structures Laboratory of Milan Polytechnic University, by using an INSTRON 8862 universal testing machine, working under *CMOD* control with a speed of 1 μm/min. The effective geometry of the three considered specimens is depicted in Figure 9a; as can be observed, a notch has been made in the central part of the bottom edge, so as to guide the crack location. A clip gauge has been fixed to the mouth of the notch, in order to control and measure the crack opening *w* during the tests (Figure 9b). Moreover, deflection $\delta$ has been measured through a LVDT transducer applied on a specific device fixed onto supports; at the same time, also the press displacement $\delta_S$ has been recorded. More details about specimen geometry and notch dimensions are reported in Table 1.

In order to observe the cracking onset and propagation, an ESPI measurement system [18] has been used. This system adopts a 20 mW Helium-Neon (HeNe) laser, which operates at a wavelength of $\lambda$ = 632.8 nm in the red part of the visible spectrum. The adopted optical setup, which has been mounted to observe horizontal displacements, is showed in Figure 10. As can be seen, the ray generated by the light source is splitted into two identical beams by a beam-splitter. Each of these beams is deviated through mirrors along a different path and hits the specimen surface with the same incidence angle with respect to its normal (Figure 10a). Passing through 40×

microscope lens, the light beams are converted into spherical waves, which reach the specimen surface illuminating a circular area with 150 mm diameter. The mutual interference of these wave fronts creates a dotted pattern, called speckle, on the illuminated surface. When the specimen undergoes a deformation the illuminated surface changes, and consequently also the speckle pattern varies. The resulting images are recorded by a CCD camera and digitally acquired through an image processing system with frame grabber interface. Then, the fringe patterns are obtained as the difference (in terms of pixel intensity values) between the current image and the initial reference image. These fringes can be regarded as contour lines representing the incremental displacement of the illuminated surface with respect to the reference image (Figure 11), with an accuracy greater than 0.1 μm. However, the deduction of displacement field from the fringe pattern is not straightforward, since it requires to count the full fringes (representing the locus of points characterized by the same displacements) of each image and multiply them for a coefficient depending on the ESPI setup. Automatic methods for this procedure, called unwrapping, could be otherwise performed [19]. Anyway, in this work ESPI images have been qualitatively read so as to determine cracking onset and crack depth $h_w$, while crack width $w$ has been deduced just on the basis of clip-gauge measurements.

Figures 11a-c report the experimental curves obtained for the three investigated AAC beams in terms of load $P$ vs. midspan deflection $\delta$ and the ESPI images corresponding to the attainment of cracking and peak loads (respectively indicated as $P_{cr}$ and $P_u$). On the same Figures the crack depth $h_w$ at peak, as deduced from ESPI images, as well as the measured fracture energy $G_F$ are also indicated for each specimen. More in details, fracture energy has been determined as the total work of fracture $W$, given by the area under the complete load $P$ - displacement $\delta$ curve, divided by the ligament area; the work done by the self weight has been properly subtracted. As can be seen, while the results of the first two tests (BB1 and BB2) are similar to each others, also in terms of fracture energy (approximately equal to 4.7 N/m), those obtained from the third specimen BB3 are instead anomalous, since the softening branch is less steep, so providing an almost double value of the fracture energy.

### *3.2 Calibration of a proper cohesive law through inverse XFEM analysis*

The so obtained results have been subsequently numerically elaborated so as to calibrate a proper cohesive law suitable for the investigated material, by performing an inverse extended finite element (XFEM) analysis.

The extended finite element method has been here preferred since it eases the difficulties in solving problems with localized features (e.g., the presence of a main crack) that are not efficiently resolved by mesh refinement. XFEM represents indeed an extension of the conventional FE method based on the concept of partition of unity [20], which takes into account a priori the discontinuous structure of the displacement field [21, 22]. Enrichment functions connected to additional degrees of freedom are added to the finite element approximation in the region of the mesh where the crack is located. These enrichment functions usually consist of the asymptotic crack tip functions that capture the singularity at the crack tip and a discontinuous function that represents the gap between the crack surfaces [e.g., 23-25]. A key advantage of this procedure is that the finite element mesh does not need to be updated to track the crack path, providing at the same time a good approximation of the displacements and, generally, leading to symmetric stiffness matrices. Since its introduction, XFEM has been subjected to different developments and improvements. As an example, in the last ten years it has been combined with cohesive crack models so allowing the simulation of fracture in quasi-brittle heterogeneous materials [26, 27]. Other developments have regarded the simulation of crack propagation in composite materials [28] and the combination of XFEM with other techniques so as to increase the rate of convergence (e.g., cut off functions and geometric enrichment, [29, 30]). Moreover, several researches have been devoted to the solution of numerical and technical problems, mainly related to enrichment implementation, as well as to the assembly of the stiffness matrix (which requires integration of singular/discontinuous functions) and to the quadrature of the weak form (among others, e.g., [31-34]). Traditional quadrature techniques, which are successfully adopted for standard finite elements, should be indeed modified when the approximation space is enriched by singular/discontinuous functions, since inaccurate quadrature can lead to poor convergence and inaccuracy in the solution.

Besides current research developments, standard XFEM is currently available in widely diffused general purpose codes, as the one (ABAQUS, [35]) used in this work to perform numerical simulations.

In this paper standard XFEM inverse analyses have been first performed on AAC beams, so as to study crack propagation (experimentally observed through ESPI technique), as well as to calibrate a proper cohesive law for the material. To this scope, according to Figure 9a and Table 1 (which are relative to experimental samples), an AAC beam with nominal dimensions equal to 620 x 100 x 250 mm has been modelled, with a 15 mm deep central notch. The presence of the notch has been accounted in numerical modeling by inserting a seam crack with the same dimensions and in the same position as the notch itself (a seam defines an edge in the model that is originally closed but can open during the analysis, due to the presence of overlapping duplicate nodes).

The beam has been discretized with 4 nodes plane stress elements with reduced integration (CPS4R in the adopted FE code library). A structured mesh has been adopted, by using 2.5 mm side square elements. To simulate the interaction between the AAC beam and the supporting steel plates, as well as between the plates and the steel rollers, an interface law has been defined, based on the measured friction coefficients (which have been set respectively equal to 0.7 for the steel-steel interface and 0.3 for the steel-AAC interface). AAC has been treated as a linear elastic material both in the tension and compression regime, by assuming the same values of elastic modulus $E$ and Poisson coefficient $\nu$ already described in § 2.2 ($E = 1320$ MPa, $\nu = 0.38$ MPa). Mechanical nonlinearities have been taken into account through the XFEM-based cohesive segments method [27], which allows to model cracking growth along an arbitrary, solution-dependent path in the material (crack position is indeed not tied to the element boundaries in the mesh). The discontinuity of the cracked elements is represented by introducing phantom nodes, which are superposed on the original real nodes [35]. When the element is intact, each phantom node is completely constrained to its corresponding real node; otherwise, when the element is cut through by a crack, the cracked element splits into two parts. Each phantom node and its corresponding real node are no longer tied together and can move apart. The magnitude of the separation is governed by the cohesive law until the cohesive strength of the cracked element is zero, after which the phantom and the real nodes move independently.

The behavior of XFEM-based cohesive segments for a crack propagation analysis is governed by the traction-separation model available in ABAQUS [35], which assumes an initially linear elastic behavior followed by the initiation and evolution of damage. More in details, when stresses or strains satisfy specified crack initiation criteria, the cohesive response at an enriched element begins to degrade, so determining crack initiation. In this work, the crack initiation criterion based on the maximum principal stress has been chosen, and consequently the process of degradation is assumed to start when the maximum principal stress attains the direct tensile strength of AAC. Subsequently, crack propagation is handled through a damage evolution law describing the rate at which the cohesive stiffness is degraded during the analysis.

In the performed numerical analysis, the direct tensile strength of AAC has been set equal to $f_{ct} = 0.54$ MPa, in order to correctly represent the mean value of the cracking load $P_{cr}$ registered during the three tests (reported in Fig. 11a-c). As can be seen, this value of direct tensile strength $f_{ct}$ is approximately equal to 0.9 $f_{ct,fl}$, being $f_{ct,fl}$ the flexural tensile strength provided by three-point bending tests on beams. For the cohesive law, an exponential relation has been chosen, having the form:

$$\sigma = [1 - d(w)] \cdot f_{ct} \tag{4}$$

where $\sigma$ is the cohesive stress, $f_{ct}$ the direct tensile strength of AAC and $d$ is a damage parameter having the form:

$$d(w) = \frac{1 - e^{-\alpha \cdot \frac{w}{w_u}}}{1 - e^{-\alpha}} \tag{5}$$

being $w_u$ the failure displacement, set equal to 0.08 mm, and $\alpha = 5$ an exponential parameter. These latter variables have been calibrated so as to obtain the mean experimental value of fracture energy $G_F$ (Figs. 11a-c). This exponential law has been plotted in Figure 11d, where it is also compared with other bilinear strain-softening relations for AAC based on experimental wedge-splitting tests (on specimens characterized by an average density of about 400 kg/m$^3$), available in the literature [4].

In order to trace the softening branch, the numerical analysis has been performed by adopting the Riks method [36]. The comparison between the so obtained numerical curve and the experimental ones is reported in Figure 12a, in terms of applied load $P$ vs.

crack mouth opening displacement *CMOD*. As can be seen, the good agreement between calculated and experimental responses suggests that the adopted exponential law is able to realistically describe crack formation and propagation in AAC. Finally, Figure 12b shows a comparison between experimental and numerical crack pattern at peak load (point A in Fig. 12a). More in details, the ESPI image has been compared to the crack pattern provided by the extended finite element analysis in terms of the variable STATUSXFEM, representing the status of each enriched element in the mesh. In particular, this variable is equal to 1 if the element is completely cracked, 0 if the element contains no crack and it is variable between 1 and 0 if the element is partially cracked. As can be seen, the adopted XFEM procedure is able to correctly represent crack propagation into the AAC matrix, also providing a good estimate of crack depth $h_w$.

## 4. AAC DEEP-BEAMS BEHAVIOR: EXPERIMENTAL TEST AND NUMERICAL MODELING BY XFEM

In order to further validate the proposed approach, an additional three-point test has been carried out under *CMOD* control on an AAC deep-beam; also in this case, the ESPI setup has been used so as to observe cracking onset and propagation. Figure 13a shows the effective geometry of the considered specimen, characterized by the presence of a notch in the central part of its bottom edge; this permits a symmetric behavior avoiding mixed mode cracking complications. The adopted test instrumentation is the same already described in the previous paragraph for beams. The obtained experimental curve is reported in Figure 13b in terms of applied load $P$ vs. midspan deflection $\delta$; the same Figure also shows the ESPI images corresponding to the cracking load $P_{cr}$, as well as to a load equal to 15.6 kN, at which the crack tip exits from the visual field. Consequently, in this case it has not been possible to measure the crack depth corresponding to the peak load $P_u$.

This experimental test has been subsequently modeled by XFEM, by following the same procedure already described in §3.2. Also in this case a structured mesh formed by 5 mm side square CPS4R elements has been adopted. AAC mechanical behavior has been again described through a linear elastic law (assuming $E$ = 1320 MPa and $\nu = 0.38$, as for beams), coupled to the XFEM-based cohesive segments method for the modeling of cracking growth. The adopted direct tensile strength, as well as the cohesive law is the same as determined on beams (see §3.2). It should be remarked that in this case the schematization of boundary conditions is slightly different from that described for beams, since the horizontal translation of the roller was partially prevented during the test, so determining the appearance of an arch effect and an increase in the experimental peak load. In order to correctly catch these aspects, the roller has been constrained with a non-linear spring, whose stiffness has been properly calibrated on the basis of the experimental behavior of the support. The interaction between the AAC specimen and the steel plates and between these latter and the rollers has been instead schematized through the same interface laws already adopted for the beam. The analysis has been carried out under load control.

The obtained results are depicted in Figure 14a, in terms of applied load *P* vs. crack mouth opening displacement *CMOD*. As can be observed, the proposed approach allows providing a correct estimate of the peak value, even if the numerical model is not able to catch the softening branch, which is very steep. The obtained numerical crack pattern at peak is reported in Figure 14b, through the STATUSXFEM variable. Other comparisons between experimental and numerical results are shown in Figure 15 in terms of crack pattern at an applied load P = 15.5 kN (as already mentioned, for higher loads the crack tip exits from the ESPI visual field), highlighting the capability of the performed simulation to represent crack propagation. Results seem to confirm that the proposed cohesive law combined with an XFEM procedure can represent a useful tool for the modeling of cracking development in AAC walls.

## 5. CONCLUSIONS

The present work aims to investigate and model cracking development in AAC beams and deep-beams. First, the problem has been experimentally afforded, by carrying out a series of tests devoted to material characterization both in compression and in flexure (through the execution of three-point bending tests), taking into account the effect of different shapes and dimensions of the investigated samples. The so obtained results have been subsequently adopted in extended finite element analyses, in order to calibrate a proper cohesive law for AAC, suitable for the modeling of cracking onset and propagation in infill and bearing walls under static loads. The main conclusions of this work can be so summarized:

- being equal the material density and the moisture content, the statistical variability of AAC mechanical properties (compressive and tensile strengths, elastic modulus and Poisson coefficient) is rather limited (below 10%); furthermore, even changing the shape and dimensions of tested samples, the obtained values have a quite limited scatter (e.g., compressive strength of small walls is about 20% lower than that measured on standard cubes). This implies that the mechanical properties measured on standard specimens are quite representative of the behavior of full-scale walls (a correction factor should be probably introduced in some cases), as well as of the behavior of non standard specimens which can be extracted from existing buildings (these latter, in general, may be indeed different in shape and dimensions from standard samples).
- load-displacement curves obtained from three-point bending tests under *CMOD* control on AAC beams show a limited scatter and provide a value of the fracture energy $G_F$ almost equal to 5-6 N/m, which is quite similar to other results obtained in the technical literature by means of wedge-splitting tests;
- on the basis of the experimental results, an exponential cohesive law has been calibrated through inverse extended finite element analysis. This law has subsequently been applied in the simulation of a three-point test on a AAC deep-beam, whose behavior is more similar to full scale infill panels.

The proposed model appears to be able to correctly catch both the peak load and the experimental crack pattern development, as revealed by the comparison with ESPI images. The obtained cohesive law can be then applied for the analysis of full scale walls, in order to study cracking development under static loads, which is a quite common problem in residential buildings.

.

**ACKNOWLEDGEMENTS**

Mr. Matteo Riva is gratefully acknowledged for his contribution in the execution of experimental tests in Piacenza. The Authors would also sincerely thank Prof. Ivo Iori for his scientific support and motivation in this research.

## REFERENCES


[1] Limbachiya MC, Roberts JJ Eds. Proc. $4^{th}$ Int Conf on AAC - Autoclaved Aerated Concrete: innovation and development. Taylor & Francis, London, 2005.

[2] Wittmann FH Eds. Proc. $3^{rd}$ RILEM Int Symp on AAC - Advances in Autoclaved Aerated Concrete. Balkema, Rotterdam, 1992.

[3] Aroni S, De Groot GJ, Robinson MJ, Svanholm G, Wittmann FH Eds. Autoclaved aerated concrete: properties, testing and design. RILEM Recommended Practice. E&FN Spon, London, 1993.

[4] Trunk B, Schober G, Helbling AK, Wittmann FH. Fracture mechanics of autoclaved aerated concrete. Cem Concr Res 1999; 29: 855-859.

[5] Brühwiler E, Wang J, Wittmann FH. Fracture of AAC as influenced by specimen dimension and moisture. J Mat Civ Eng 1990; 2: 136-146.

[6] Wittmann FH, Gheorghita I. Fracture toughness of autoclaved aerated concrete. Cem Concr Res 1984; 14:369-374.

[7] Isu N, Teramura S, Tshida H, MitsudaT. Influence of quartz particle size on the chemical and mechanical properties of autoclaved aerated concrete (II): fracture toughness, strength and micropore. Cem Concr Res 1995; 25: 249-254.

[8] Narayanan N, Ramamurthy K. Structure and properties of aerated concrete: a review. Cem & Concr Comp 2000; 22:321-329.

[9] Valore RC. Cellular concretes - Part 2: Physical properties. J American Concr Inst 1954; 50: 817-836.

[10] Marzahn GA. Extended investigation of mechanical properties of masonry units. LACER No. 7, 2002: 237-254.

[11] Tanner JE. Design provisions for autoclaved aerated concrete (AAC) structural systems. PhD Thesis, University of Austin, Texas, 2003.

[12] Wolf S, Wiegand S, Stoyan D, Walther HB. The compressive strength of AAC – a statistical investigation. Proc. 4th Int Conf on Autoclaved Aerated Concrete: innovation and Development. Taylor & Francis, London, 2005: 287-295.

[13] Ferretti D, Michelini E, Gazzola G, Riva M, Rosati G. Cracking in AAC elements: experimental investigation with ESPI technique (in Italian). Proc. $17^{th}$ C.T.E. Congress, Rome, 2008: 409-417.

[14] Argudo JF. Evaluation and synthesis of experimental data for autoclaved aerated

concrete. PhD Thesis, University of Austin, Texas, 2003.
[15] IUAV University. Test Report n°18678 - Determination of AAC mechanical properties. Venice, 2006.
[16] UNI EN 772-1. Methods of test for masonry units - Part 1: Determination of compressive strength, 2002.
[17] UNI EN 771-4. Specification for masonry units - Part 4: Autoclaved aerated concrete masonry units, 2005.
[18] Jones R, Wykes C. Holographic and speckle interferometry. Cambridge University Press, Cambridge, 1989.
[19] Ferretti D, Rossi M, Royer-Carfagni G. An ESPI experimental study on the phenomenon of fracture in glass. Is it brittle or plastic? J Mech Phys Solids 2011; 59(7): 1338-1354.
[20] Melenk JM, Babuska I. The partition of unity finite element method: basic theory and applications. Comp Meth Appl Mech and Engng 1996; 39:289–314.
[21] Belytschko T, Gracie R, Ventura G. A review of extended/generalized finite element methods for material modeling. Model Simul Mater Sci Engrg 2009; 17(4):043001.
[22] Richardson CL, Hegemann J, Sifakis E, Hellrung J, Teran JM. An XFEM method for modeling geometrically elaborate crack propagation in brittle materials. Int J Numer Meth Engng 2011; 88: 1042-1065
[23] Belytschko T, Black T. Elastic crack growth in finite elements with minimal remeshing. Int J Numer Meth Engng 1999; 45(5): 601-620
[24] Moës N, Dolbow J, Belytschko T. A finite element method for crack growth without remeshing. Int J Numer Meth Engng 1999; 46:131–150.
[25] Gracie R, Ventura G, Belytschko T. A new fast finite element method for dislocations based on interior discontinuities. Int J Numer Meth Engng 2007; 69:423–441.
[26] Moës N, Belytschko T. Extended finite element method for cohesive crack growth. Eng Frac Mech 2002; 69:813–833.
[27] Remmers JJC, de Borst R, Needleman A. The simulation of dynamic crack propagation using the cohesive segments method. J Mech Phys Solids 2008, 56: 70–92.

[28] Huynh D, Belytschko T. The extended finite element method for fracture in composite materials. Int J Numer Meth Engng 2009; 77(2):214–239.

[29] Chahine E, Laborde P, Renard Y. Crack tip enrichment in the XFEM using a cutoff function. Int J Numer Meth Engng 2008; 75(6):626–646.

[30] Lew A, Shen Y. Crack tip enrichment in the XFEM using a cutoff function. Int J Numer Meth Engng 2008; 75(6):629–646.

[31] Ventura G, Gracie R, Belytschko T. Fast integration and weight function blending in the extended finite element method. Int J Numer Meth Engng 2009; 77(1):1–29.

[32] Benvenuti E, Tralli A, Ventura G. A regularized XFEM model for the transition from continuous to discontinuous displacements. Int J Numer Meth Engng 2008; 74(6):911–944.

[33] Benvenuti E, Ventura G, Ponara N. Finite element quadrature of regularized discontinuous and singular level set functions in 3D problems. Algorithms 2012; 5: 529-544.

[34] Benvenuti E, Ventura G, Ponara N, Tralli A. Variationally consistent eXtended FE model for 3D planar and curved imperfect interfaces. Comput Methods Appl Mech Engrg 2013; 267: 434-457.

[35] ABAQUS 6.12. Online Documentation. Dassault Systémes Simulia Corp.

[36] Crisfield M.A. Nonlinear finite element analysis of solids and structures. Vol. 1: Essentials. Wiley, New York, 1991.

## FIGURES

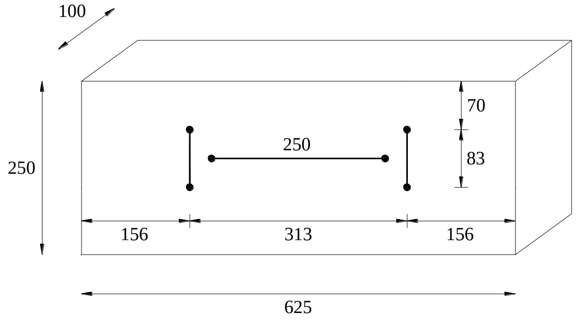


(a)


(b)

Figure 1

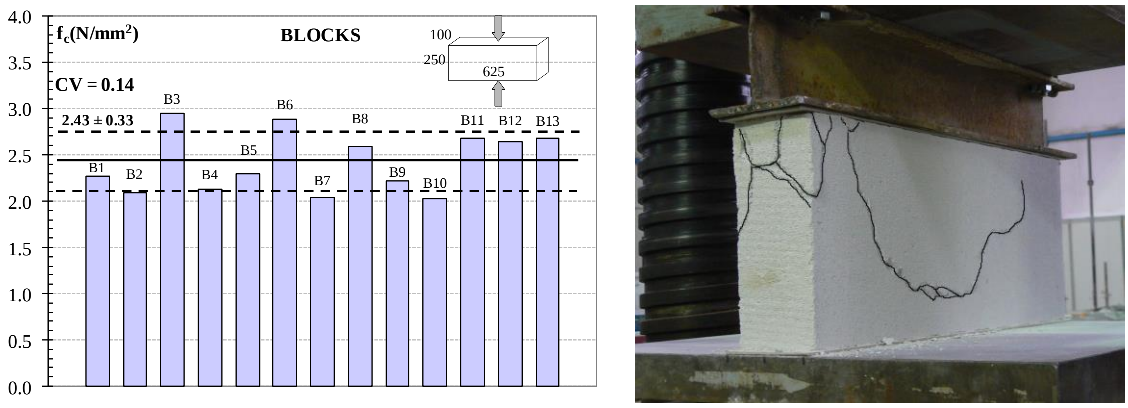

fc(N/mm2)
BLOCKS
CV = 0.14
2.43 ± 0.33
100
250
625
B1
B2
B3
B4
B5
B6
B7
B8
B9
B10
B11
B12
B13
4.0
3.5
3.0
2.5
2.0
1.5
1.0
0.5
0.0


(a) (b)

Figure 2

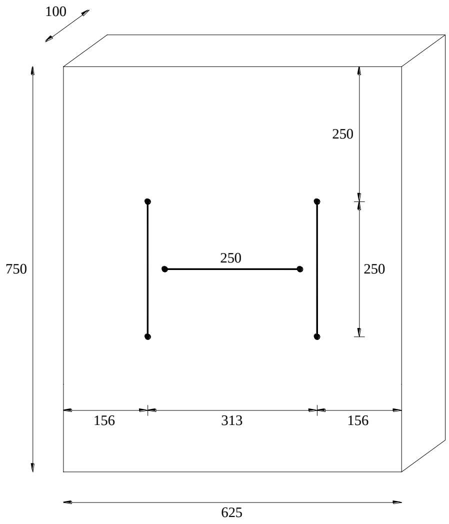


(a)


(b)

Figure 3

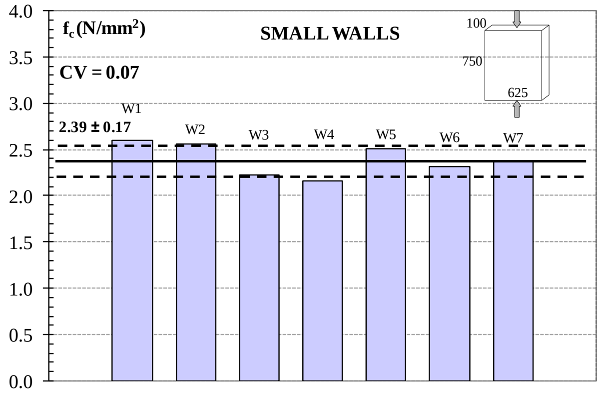
f_c (N/mm²)
SMALL WALLS
CV = 0.07
2.39 ± 0.17
100
750
625
W1
W2
W3
W4
W5
W6
W7
4.0
3.5
3.0
2.5
2.0
1.5
1.0
0.5
0.0

(a)

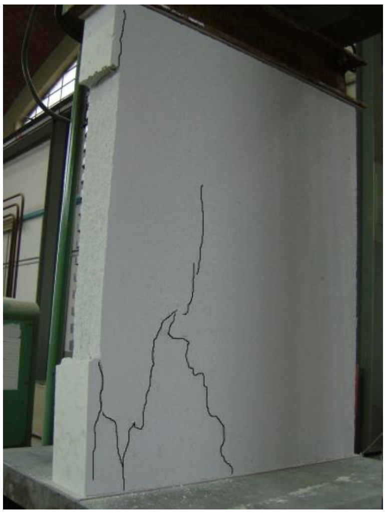

(b)

Figure 4

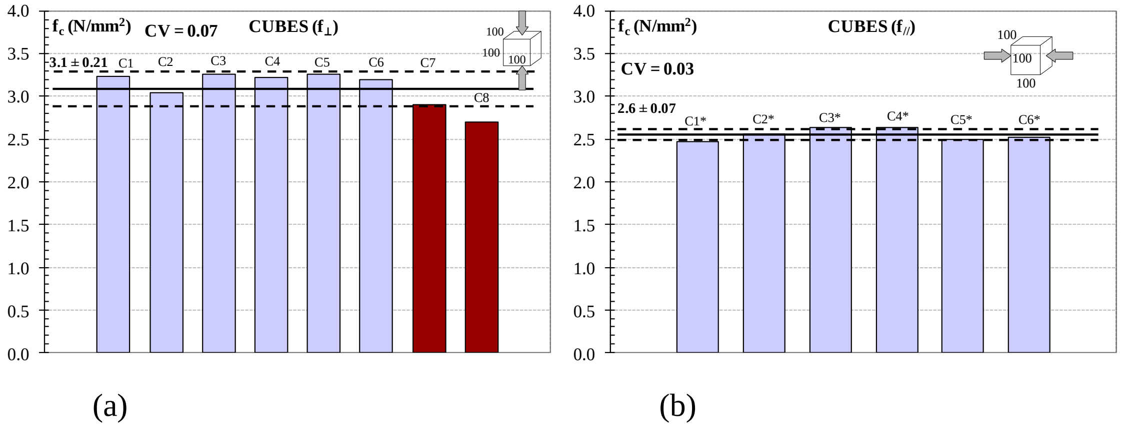

(a)
4.0
3.5
3.0
2.5
2.0
1.5
1.0
0.5
0.0
f_c (N/mm^2)
CV = 0.07
CUBES (f_⊥)
3.1 ± 0.21
C1
C2
C3
C4
C5
C6
C7
C8
100
100
100
(b)
4.0
3.5
3.0
2.5
2.0
1.5
1.0
0.5
0.0
f_c (N/mm^2)
CUBES (f_//)
CV = 0.03
2.6 ± 0.07
C1*
C2*
C3*
C4*
C5*
C6*
100
100
100


Figure 5

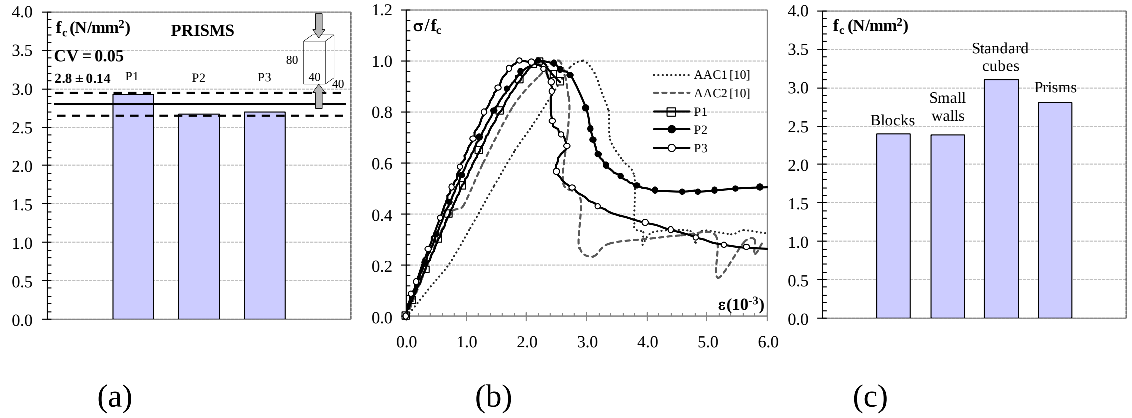

(a)
fc (N/mm2)
PRISMS
CV = 0.05
2.8 ± 0.14
P1
P2
P3
80
40
40
(b)
σ/fc
AAC1 [10]
AAC2 [10]
P1
P2
P3
ε(10-3)
(c)
fc (N/mm2)
Blocks
Small walls
Standard cubes
Prisms


Figure 6

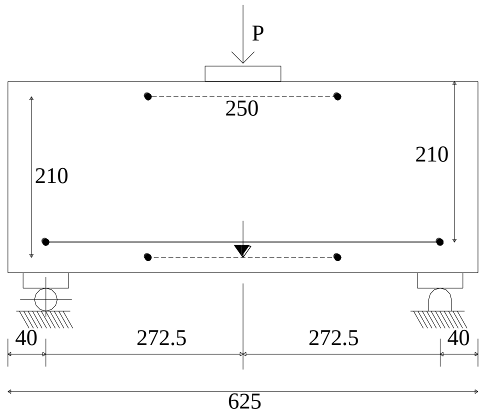


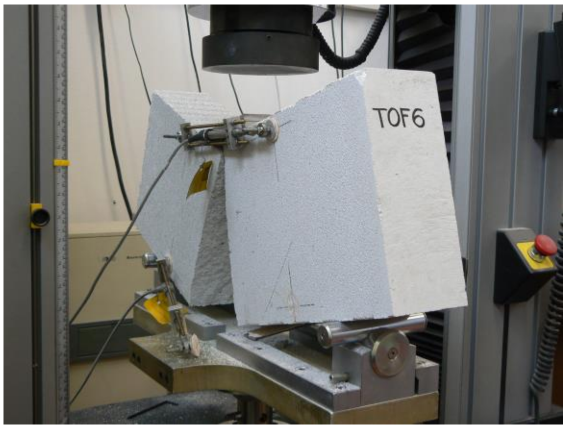


(a) (b)

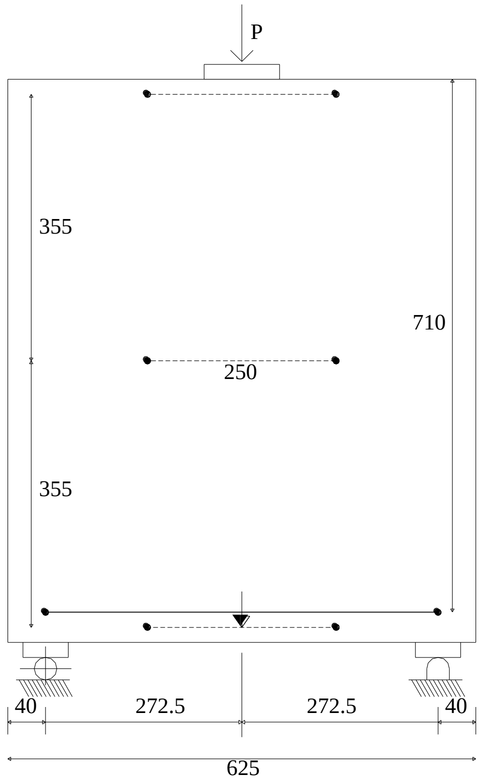


(c) (d)

Figure 7

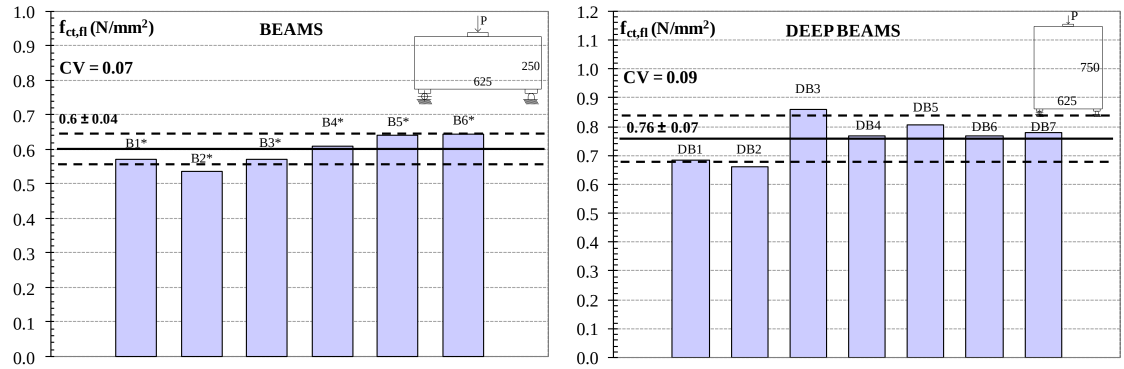

f_ct,fl (N/mm²)
BEAMS
CV = 0.07
0.6 ± 0.04
B1*
B2*
B3*
B4*
B5*
B6*
P
250
625
f_ct,fl (N/mm²)
DEEP BEAMS
CV = 0.09
0.76 ± 0.07
DB1
DB2
DB3
DB4
DB5
DB6
DB7
750
625


(a) (b)

Figure 8

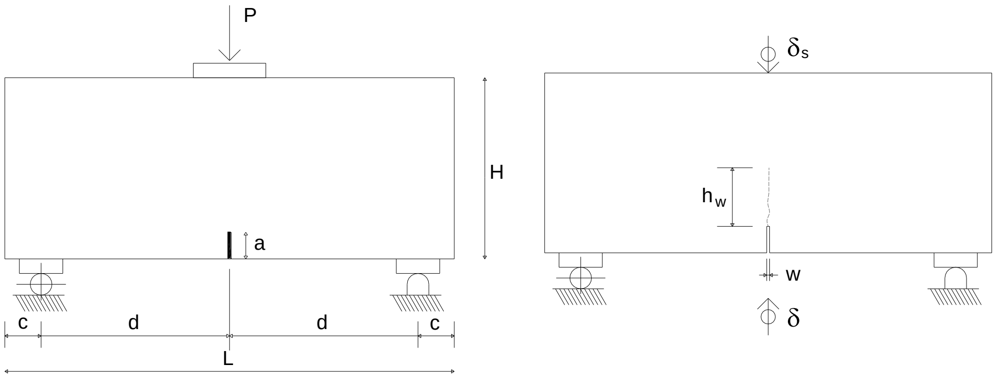


(a) (b)

Figure 9

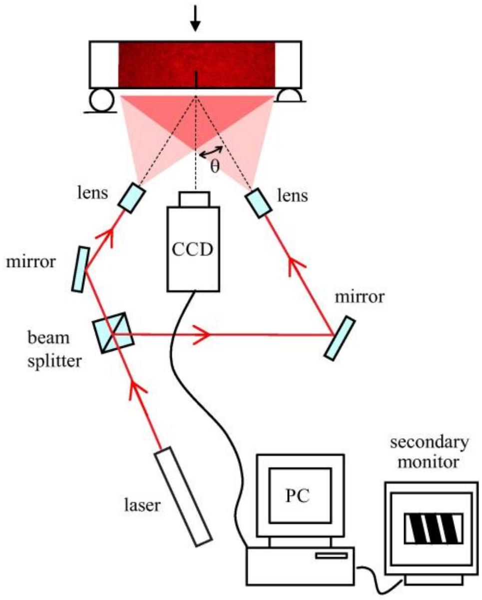

θ
lens
lens
CCD
mirror
mirror
beam
splitter
secondary
monitor
PC
laser


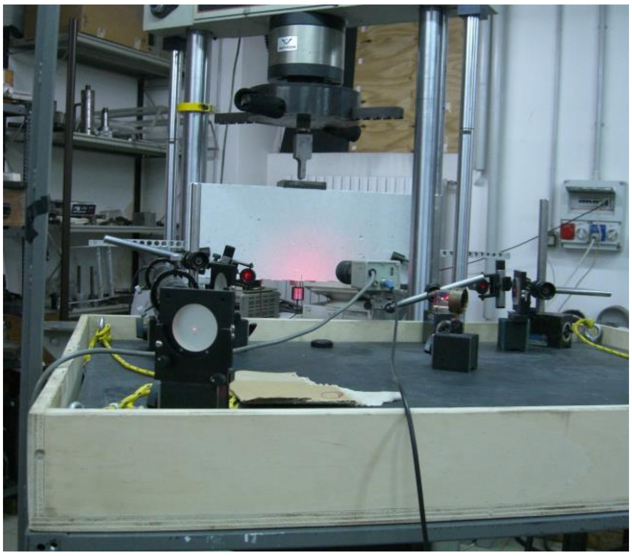

(a) (b)

Figure 10

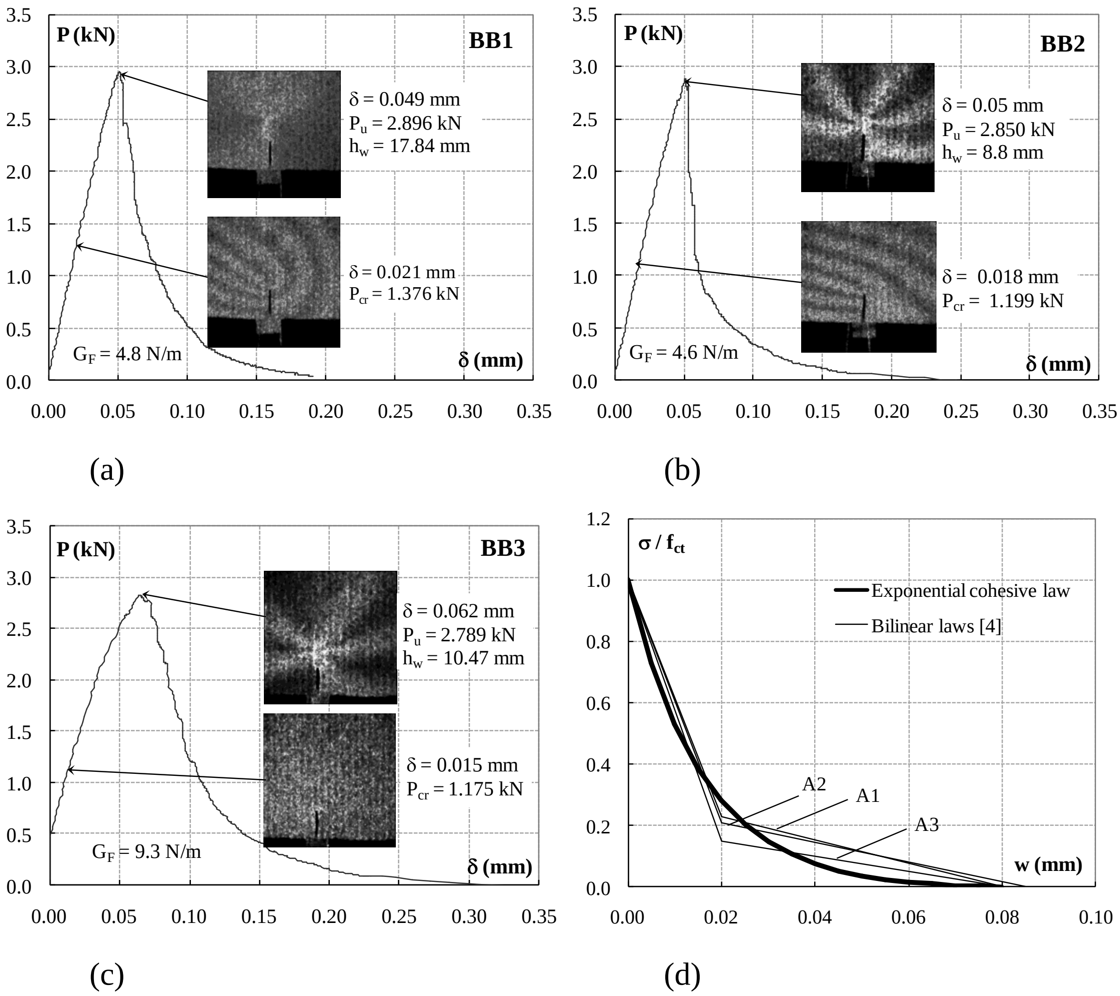

P (kN)
BB1
δ = 0.049 mm
Pu = 2.896 kN
hw = 17.84 mm
δ = 0.021 mm
Pcr = 1.376 kN
GF = 4.8 N/m
δ (mm)
(a)
P (kN)
BB2
δ = 0.05 mm
Pu = 2.850 kN
hw = 8.8 mm
δ = 0.018 mm
Pcr = 1.199 kN
GF = 4.6 N/m
δ (mm)
(b)
P (kN)
BB3
δ = 0.062 mm
Pu = 2.789 kN
hw = 10.47 mm
δ = 0.015 mm
Pcr = 1.175 kN
GF = 9.3 N/m
δ (mm)
(c)
σ / fct
Exponential cohesive law
Bilinear laws [4]
A2
A1
A3
w (mm)
(d)


Figure 11

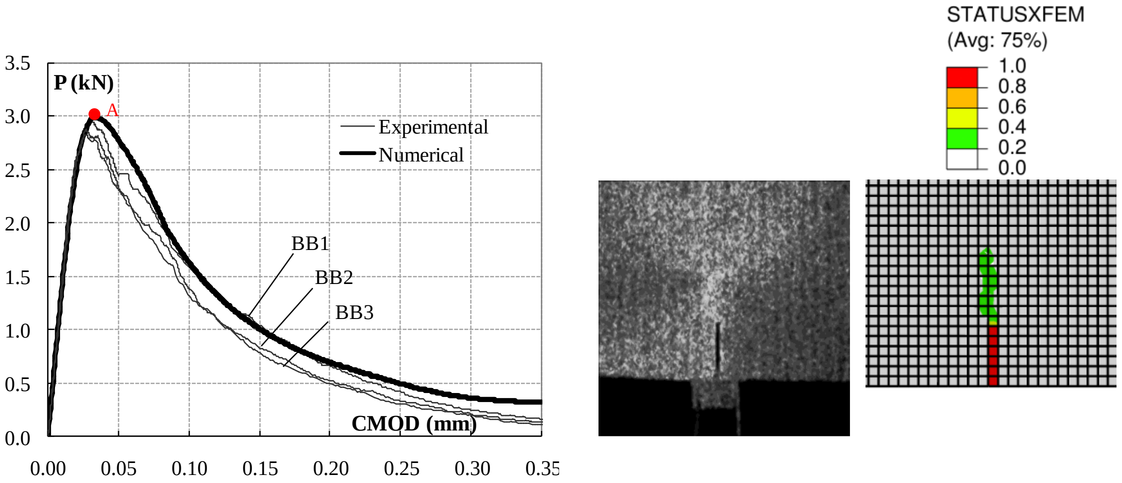
P (kN)
3.5
3.0
2.5
2.0
1.5
1.0
0.5
0.0
A
Experimental
Numerical
BB1
BB2
BB3
CMOD (mm)
0.00
0.05
0.10
0.15
0.20
0.25
0.30
0.35
STATUSXFEM
(Avg: 75%)
1.0
0.8
0.6
0.4
0.2
0.0

(a) (b)

Figure 12

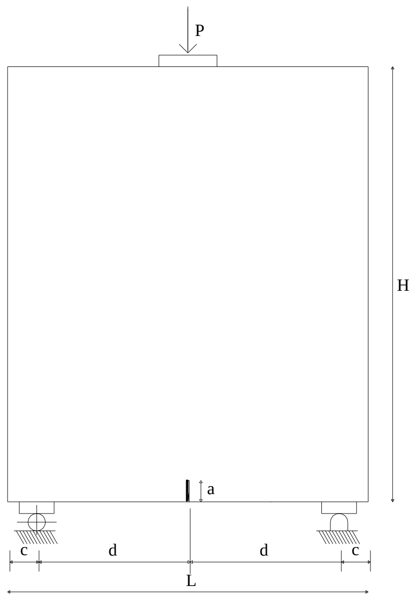


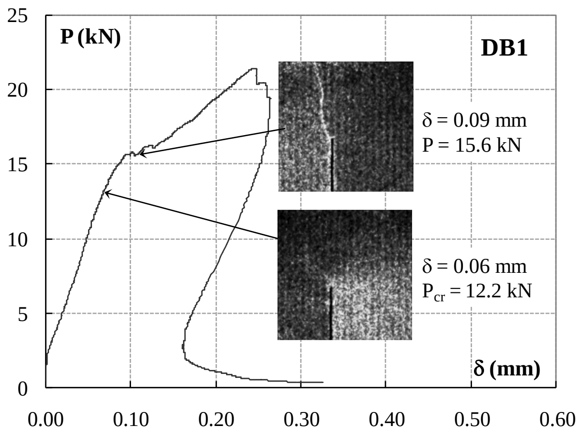


| **Specimen ID** | DB1 |
|---|---|
| **L x H x b (mm)** | 624 x 748 x 100 |
| **a (mm)** | 30 |
| **c (mm)** | 40 |
| **d (mm)** | 272 |

(a) (b)

Figure 13

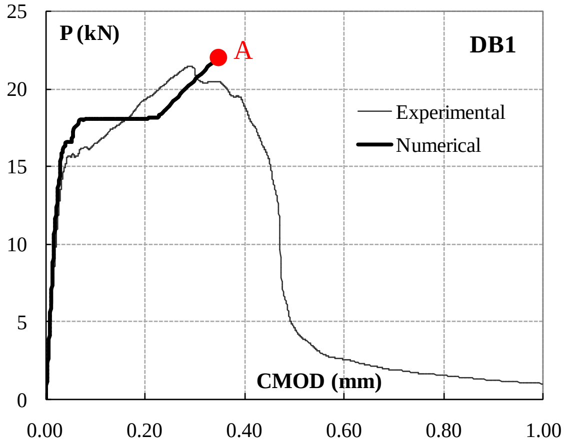

25
P (kN)
DB1
A
20
Experimental
Numerical
15
10
5
0
CMOD (mm)
0.00
0.20
0.40
0.60
0.80
1.00

(a)

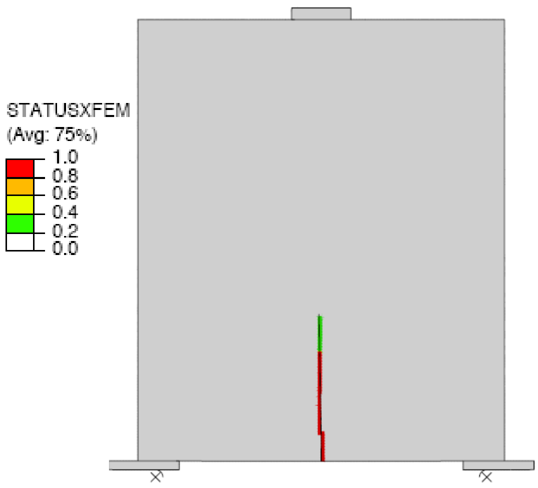

STATUSXFEM
(Avg: 75%)
1.0
0.8
0.6
0.4
0.2
0.0

(b)

Figure 14

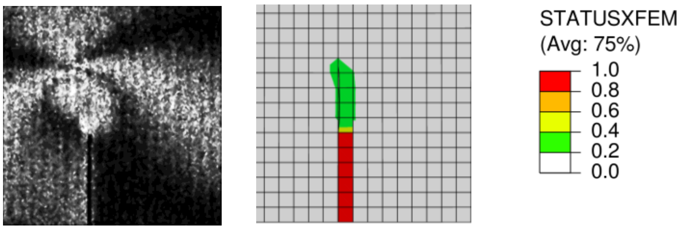


Figure 15

## TABLES

| Specimen ID | L x H x b (mm) | a (mm) | c (mm) | d (mm) |
|---|---|---|---|---|
| BB1 | 620 x 251.1 x 99.20 | 14.5 | 40.0 | 270.0 |
| BB2 | 620 x 251.2 x 100.1 | 12.0 | 40.0 | 270.0 |
| BB3 | 620 x 251.3 x 100.1 | 12.0 | 40.0 | 270.0 |

Table 1

**LIST OF FIGURES AND TABLES**

beams with 625 mm x 100 mm basis and 250 mm high; (b) deep-beams with 625 mm x 100 mm basis and 750 mm high.

Figure 9. Three-point bending tests on AAC beams under *CMOD* control: (a) specimen geometry and (b) variables measured during the test.

Figure 10. (a) ESPI optical setup; (b) adopted test arrangement.

Figure 11. Experimental load $P$ - deflection $\delta$ curves and ESPI images corresponding to cracking load $P_{cr}$ and peak load $P_u$ for the three investigated AAC beams: (a) BB1, (b) BB2, (c) BB3; (d) comparison between the adopted exponential cohesive law and relations proposed in [4] for AAC.

Figure 12. AAC beams: (a) comparison between numerical and experimental curves in terms of applied load $P$ vs. crack mouth opening displacement *CMOD*; (b) comparison between experimental and numerical crack pattern at peak load (point A).

Figure 13. Three-point bending test on a AAC deep-beam under *CMOD* control: (a) specimen geometry and dimensions; (b) experimental load $P$ - deflection $\delta$ curve and ESPI images corresponding to cracking load $P_{cr}$ and to a load $P$ = 15.6 kN.

Figure 14. AAC deep-beam: (a) comparison between numerical and experimental curves in terms of applied load $P$ vs. crack mouth opening displacement *CMOD*; (b) numerical crack pattern at peak load (point A).

Figure 15. AAC deep-beam: comparison between experimental and numerical crack pattern for an applied load P = 15.5 kN.

Table 1. Effective dimensions of tested specimens and depth of the notch.